



# Deformation and strengthening mechanisms of a carbon nanotube reinforced aluminum composite



F. Mokdad<sup>a</sup>, D.L. Chen<sup>a,\*</sup>, Z.Y. Liu<sup>b</sup>, B.L. Xiao<sup>b</sup>, D.R. Ni<sup>b</sup>, Z.Y. Ma<sup>b,\*\*</sup>

<sup>a</sup> Department of Mechanical and Industrial Engineering, Ryerson University, 350 Victoria Street, Toronto, Ontario, M5B 2K3, Canada

<sup>b</sup> Shenyang National Laboratory for Materials Science, Institute of Metal Research, Chinese Academy of Sciences, 72 Wenhua Road, Shenyang, 110016, China

## ARTICLE INFO

### Article history:

Received 15 January 2016

Received in revised form

12 March 2016

Accepted 17 March 2016

Available online 22 March 2016

## ABSTRACT

The objective of this study was to characterize microstructure, texture, and deformation behavior of a carbon nanotube (CNT) reinforced aluminum composite via electron backscatter diffraction (EBSD), X-ray diffraction (XRD), scanning and transmission electron microscopy. The addition of 2.0 wt.% CNTs in a 2024Al alloy led to considerable grain refinement, with a bi-modal distribution of grain misorientation angles positioned at  $\sim 7^\circ$  for low-angle grain boundaries and  $\sim 50^\circ$  for high-angle grain boundaries. The CNTs were observed to be uniformly dispersed in the matrix while some CNT shortening occurred during ball milling. The grain size reduction and compressive micro-strains in the composite broadened X-ray peaks and resulted in lattice shortening. The macro-texture determined via XRD and micro-texture via EBSD were in good agreement, revealing that the composite contained stronger  $\{112\} \langle 111 \rangle$  Copper texture and  $\{110\} \langle 001 \rangle$  Goss texture in comparison with 2024Al base alloy. The deformation resistance of the composite at both room and elevated temperatures was effectively enhanced due to the CNT addition. This was mainly attributed to the role of underlying strengthening mechanisms: Hall-Petch strengthening (significant grain refinement involving the Zener pinning effect of CNTs), and composite strengthening including load transfer, thermal mismatch and Orowan looping.

© 2016 Elsevier Ltd. All rights reserved.

## 1. Introduction

Carbon nanotubes (CNTs) are considered as attractive reinforcements for aluminum matrix composites (AMCs) due to their excellent mechanical and physical properties as well as light weight [1–3]. CNT reinforced AMCs are promising materials in a variety of areas (e.g., in the aerospace, thermal management, and automotive sectors) [4]. However, there are still several challenging issues that need to be resolved including interfacial reactions, low wettability, and anisotropic properties [5]. Investigations in the past have mainly been conducted on the CNT reinforced polymer or ceramic matrix composites. Among the first studies on the CNT/Al composite, Kuzumaki et al. [6] characterized the elastic and plastic responses. More studies were later focused on the synthesis and processing techniques of the composites. For instance, Bustamante et al. [7] studied a 2024Al alloy which was produced by mechanical alloying and strengthened by CNT dispersion. Liu et al. [8]

combined powder metallurgy with subsequent friction stir processing (FSP), and reported well-retained layer structures of the CNTs.

Mechanical testing is required to establish the structure-property relationships of the composites; however, most of the studies in the literature [9–12] involved the tensile behavior of the CNT/Al composites at room temperature (RT). Nanocomposites and other structural materials could be subjected to either tensile or compressive forces at varying temperatures when used in systems and devices. Silvestre et al. [12] studied the mechanical behavior of CNT/Al composites under compression using molecular dynamics and noted the sensitivity of CNTs under compression to buckling and kinking. Several other studies on the compressive behavior of CNT reinforced composites indicated the beneficial role of CNT additions [13–15]. For instance, Bakshi et al. [14] observed a significant improvement in the compressive yield strength by 27% and 77% at RT through the addition of 5.0 and 10.0 wt.% CNTs, respectively. It is however unclear whether this improvement would sustain at higher temperatures and how the compressive behavior of CNT reinforced composites would change with deformation temperature.

\* Corresponding author.

\*\* Corresponding author.

E-mail addresses: [dchen@ryerson.ca](mailto:dchen@ryerson.ca) (D.L. Chen), [zyma@imr.ac.cn](mailto:zyma@imr.ac.cn) (Z.Y. Ma).

While some limited microstructural studies on the CNT reinforced Al composite were reported in the literature [7,16,17], three-dimensional electron backscatter diffraction (EBSD) investigations along different observational planes of the composite are not available, to the authors' knowledge. While the compressive microstrains were noted to occur in the CNT reinforced composites [17–19], which would result in X-ray diffraction peak broadening, no actual quantification of the resultant lattice change is reported. It is hence necessary to understand how the addition of CNTs affects the lattice change, microstructure and texture, and especially what strengthening mechanisms are involved. Therefore, the main objectives of this study were to examine the microstructural features and alterations coming from the CNT addition, evaluate the compressive deformation behavior of the 2.0 wt.% CNT/2024Al composite at varying strain rates and temperatures, and identify the salient strengthening mechanisms.

## 2. Material and experimental procedure

The studied material consisted of 2.0 wt.% CNTs mixed with 2024Al alloy powders having a composition (in wt.%) of 4.5 Cu, 1.5 Mg, 0.6 Mn, and Al (balance). The average diameter of the 2024Al powders was  $\sim 10\ \mu\text{m}$ . The as-received CNTs (95–98% purity) were synthesized using chemical vapor deposition (CVD). CNTs had entangled morphologies with a length of  $>5\ \mu\text{m}$  and an outer diameter of 10–20 nm. The as-mixed powders of 2024Al and 2.0 wt.% CNTs were dispersed by ball milling for 6 h at a rotational speed of 400 RPM and a ball powder ratio of 15:1, using a stir milling machine with hardened steel balls of 5 mm in diameter. No extra pre-treatment was conducted on the CNTs before milling, however 2.0 wt.% stearic acid was added to prevent serious cold-welding. The as-milled powders were cold-compacted in a cylinder die, degassed, then hot pressed at  $560\ ^\circ\text{C}$  for 1 h into cylindrical billets. The as-pressed billets were hot extruded at  $450\ ^\circ\text{C}$  with a ratio of 25:1. The 2.0 wt.% CNT/2024Al composite was finally solid-solution-treated at  $495\ ^\circ\text{C}$  for two hours, quenched in water at RT and then naturally aged (i.e., equivalent to the T4 condition). Cylindrical specimens with a diameter of 5 mm and a height of 8 mm in concordance with ASTM E9–09 standard were prepared, with the compression axis parallel to the extrusion direction (ED). Compression tests were carried out until failure at RT,  $200\ ^\circ\text{C}$ ,  $300\ ^\circ\text{C}$  and  $400\ ^\circ\text{C}$ , at strain rates of 0.001, 0.01, 0.1 and  $1\ \text{s}^{-1}$ , using a computerized United testing machine equipped with an environmental chamber having a temperature accuracy of  $\pm 5\ ^\circ\text{C}$ . Samples were first heated up to the test temperatures and held for 300 s in order to maintain a steady deformation temperature. A calibration curve at each temperature was obtained to get rid of the machine deformation in evaluating the stress–strain curves. To verify the reproducibility of the results, two tests were performed for each combination of strain rate and deformation temperature.

An optical microscope equipped with an image analysis system, and a scanning electron microscope (SEM) JSM-6380LV along with an Oxford energy dispersive X-ray spectroscopy (EDS) system, were used to observe microstructures. CNT distributions and CNT–Al interface structures in the matrix were examined using transmission electron microscopy (TEM, Tecnai G2 20) and high resolution TEM (HRTEM). The TEM samples were prepared to be paralleled to the ED. EBSD analyses were carried out at a step size of  $0.1\ \mu\text{m}$  by means of Oxford integrated AZtecHKL advanced EBSD system with NordlysMax<sup>2</sup> and AZtecSynergy along with a large area analytical silicon drift detector. To characterize the initial microstructures, samples were polished via standard metallographic techniques. To obtain the optical micrographs, microstructural features were revealed using Keller's etchant (i.e., 190 ml H<sub>2</sub>O, 5 ml HNO<sub>3</sub> (65%), 3 ml HCl (32%) and 2 ml HF (40%)). No etching was

done for the SEM observations, where the polished surfaces were examined directly. As for the EBSD examinations, sample surface was first mechanically polished, then electro-polished in an electrolyte of 10 ml nitric acid and 40 ml ethanol for about 30 s at 20 V and RT. Crystallographic texture was determined with a PANalytical X-ray diffractometer (XRD) with Cu K $\alpha$  radiation at 45 kV and 40 mA in a back reflection mode by measuring partial pole figures (i.e., ranging between  $\Psi = 0^\circ$  and  $75^\circ$ ). The correction of the defocusing coming from the rotation of XRD sample holder was made using the experimental data obtained from aluminum powder diffraction. Texture data obtained via XRD were subsequently evaluated using the Matlab-based MTEX software. EBSD data were analyzed by means of the AZtecHKL EBSD data acquisition software of Oxford Instruments.

## 3. Results

### 3.1. Microstructure and EBSD analysis

Fig. 1(a) shows a three-dimensional optical micrograph of the 2.0 wt.% CNT/2024Al composite, where each of the studied surfaces (i.e., parallel and perpendicular to the ED) was prepared separately, then assembled together to visualize the shape of a compression-like test specimen. While some elongated grains were seen on the surface parallel to the ED, equiaxed grains were observed on the cross section. Likewise, two surfaces parallel and perpendicular to the ED were each examined via EBSD, and then combined together to present a three-dimensional orientation map in Fig. 1(b). Map color legend was projected towards the ED on the cylinder surface and towards the radial direction (RD) on the cross-section. It is seen from the surface parallel to the ED that the larger elongated grains mainly exhibited a  $\langle 111 \rangle$  texture (blue color), with a few elongated grains orientated in the  $\langle 001 \rangle$  direction (red color). On the cross section, while some  $\langle 111 \rangle$  and  $\langle 001 \rangle$  colors could be seen, most equiaxed grains exhibited more randomized orientations or assorted colors.

Similarly, Fan et al. [20] studied the EBSD maps of a laminated CNT/7055Al composite and indicated the presence of a strong

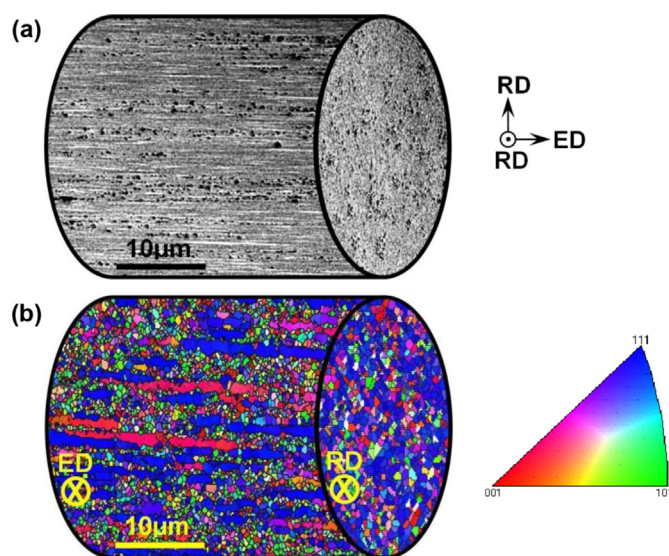


**Fig. 1.** Three-dimensional image of (a) optical microstructure and (b) EBSD orientation map of the 2.0 wt.% CNT/2024Al composite, where ED and RD stand for the extrusion and radial directions, respectively. Map color legend is projected towards the ED on the cylinder surface and towards the RD on the cross-section. (A colour version of this figure can be viewed online.)

<111> fiber texture. This orientation was indeed recognized as a hard orientation in the face centered cubic (FCC) crystal structure, in direct relation to the normal {111}<110> slip systems [21]. As expected, the presence of the elongated grains along the ED shown in Fig. 1 was attributed to the severe plastic deformation during extrusion. In this context, Liao et al. [22] studied the microstructures of various Al powders reinforced with 0.5 wt.% CNT and showed that the microstructural features of the composite were highly dependent on the deformation process. The as-sintered specimens had initially equiaxed grains, which were then elongated when subjected to a hot-extrusion process.

Since the present study strongly relies on the findings of EBSD analysis, and knowing the challenges for obtaining accurate EBSD results from MMCs [23–25], point-by-point mean angular deviation (MAD) histograms were evaluated and shown in Fig. 2. These histograms provided information about the mean of the deviations from the measured angles from the pattern, and the ideal angles calculated from the loaded crystal structure. The larger the MAD was, the poorer the fit of the solution to the pattern was [26]. If the MAD for a pattern during mapping was greater than  $1^\circ$ , the pixel would be poorly solved. The more deformed the sample was, the harder it was to get a perfect misfit. As seen from Fig. 2(a), only a small portion of MAD values was larger than  $1^\circ$  for 2024Al, which was considered as a reference. Although slightly poorer results were observed for the 2.0 wt.% CNT/2024Al (Fig. 2(b)) compared with the case of 2024Al, a majority of MAD values was still smaller than  $1^\circ$ , suggesting that the fit of the solution to the pattern for the composite was acceptable.

A close examination on the 3D image in Fig. 1(a) indicated the presence of second phase particles in the 2.0 wt.% CNT/2024Al composite. Thus, SEM observations were conducted in comparison with the 2024Al alloy for more details. Fig. 3 shows the SEM micrographs for the 2024Al (Fig. 3(a) and (b)) and the 2.0 wt.% CNT/2024Al (Fig. 3(c) and (d)).

Both base alloy and composite displayed some coarser particles indicated by the thicker yellow arrows on Fig. 3(b) and (d). However, a close examination of Fig. 3(c) and (d) revealed two types of particles which could be distinguished by their distinct size and shape. Numerous uniformly distributed nanoparticles in the Al matrix were seen in the composite (as pointed out by the thinner red arrows in Fig. 3(d)), which will be further examined via TEM analysis. To understand the nature of coarser particles in the composite, EDS line scan was performed and shown in Fig. 4.

During the EDS analysis all the main alloying elements (i.e., Al, Cu, Mg, and Mn) were considered, however only Cu-containing particles were present (Fig. 4(b)). Similar results were reported by Bustamante et al. [16] who studied the microstructure of a 5.0 wt.% CNT/2024Al composite after sintering, and observed a good dispersion of  $\text{Al}_2\text{Cu}$  coarse particles due to the low cooling rate in the sintering process. The presence of this phase will be further confirmed via XRD phase analysis. The eventual presence of  $\text{Al}_2\text{O}_3$  oxides due to the spontaneous reaction between Al and  $\text{O}_2$ , when exposed to air during milling, will be also discussed later.

TEM examinations of the 2.0 wt.% CNT/2024Al composite revealed singly dispersed CNTs in the Al matrix, as indicated by the red thin arrows in Fig. 5(a). CNTs shorter than the received ones were also observed which was apparently attributed to the significant breakup in the fabrication of the composite where CNTs were shortened during milling due to shear effect. This observation was in agreement with the results obtained by Liu et al. [8] who have discussed the effect of stirring during FSP on the CNTs. The presence of  $\text{Al}_4\text{C}_3$  phase was also detected, as indicated by the blue thick arrows in Fig. 5(a), being either directly attached to CNTs or in the matrix in the vicinity of CNTs. The existence of this phase will be further corroborated via XRD analysis as well.

Fig. 5(b) presents a HRTEM image showing the interface between the Al matrix and CNT. Different features (i.e., Al, CNT, and interface) were clearly distinguished in Fig. 5(b). The CNT-Al interface was densely bonded, and no void or defects were observed. The layered carbon structure within the CNT as well as the interlayer distance between the CNT walls were visible. The coherent interface is important since the direct bond between the matrix and the reinforcement help understand the contribution of the load transfer (i.e., CNTs would carry a portion of the load between the matrix and reinforcement [11,27]) in the strengthening mechanisms of the composite. Interfacial shear stresses originating from the matrix could be transferred to the CNTs [28]. The presence of  $\text{Al}_4\text{C}_3$  phase at the interface (Fig. 5(a)) was also reported to be essential for an effective load transfer between the matrix and CNTs [29,30]. More details about the load transfer between the matrix and reinforcement will be given.

### 3.2. X-ray diffraction analysis

XRD patterns acquired from the 2024Al alloy and the 2.0 wt.% CNT/2024Al composite are presented in Fig. 6. The presence of Al

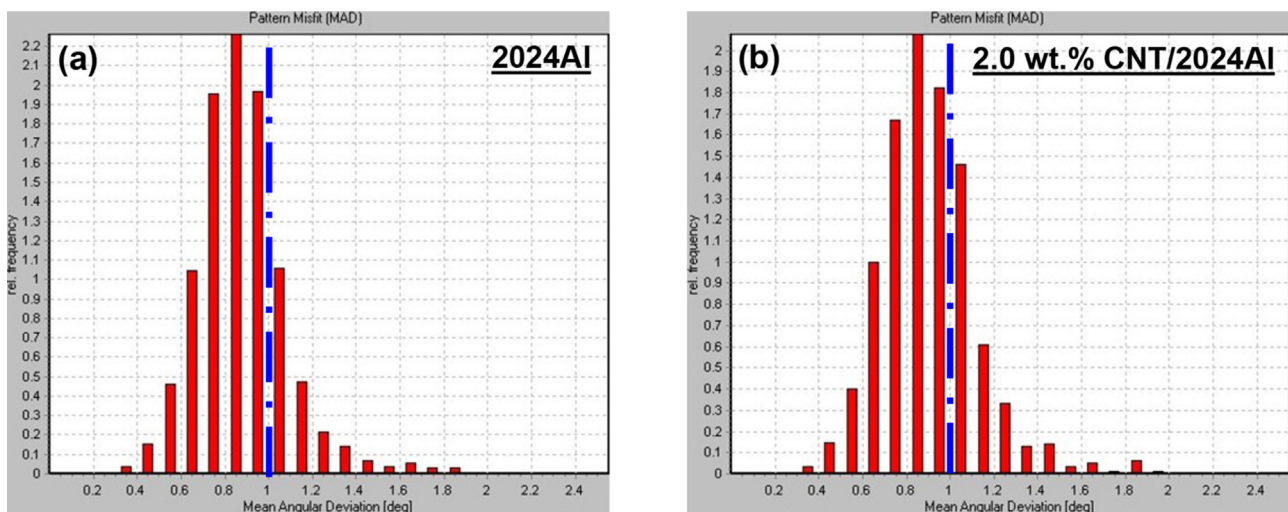


Fig. 2. Point-by-point mean angular deviation (MAD) histograms of (a) 2024Al alloy and (b) 2.0 wt.% CNT/2024Al composite. (A colour version of this figure can be viewed online.)

$$\frac{\Delta \sin^2 \theta}{\sin^2 \theta} = -2K \cos^2 \theta,$$

or

$$\Delta \sin^2 \theta = -2K \cos^2 \theta \sin^2 \theta = D \sin^2 2\theta, \quad (6)$$

with  $D$  ( $=-K/2$ ) is known as the drift constant, specific for every diffraction pattern [38].

In the Cohen's method  $\Delta \sin^2 \theta$  is considered as,

$$\Delta \sin^2 \theta = \sin^2 \theta - \sin^2 \theta_0, \quad (7)$$

where  $\sin^2 \theta_0$  could be given by Refs. [40],

$$\sin^2 \theta_0 = \frac{\lambda^2}{4a_0^2} (h^2 + k^2 + l^2). \quad (8)$$

Considering Eqs. (7) and (8), the new form of Eq. (6) becomes,

$$\sin^2 \theta - \frac{\lambda^2}{4a_0^2} (h^2 + k^2 + l^2) = D \sin^2 2\theta. \quad (9)$$

Eq. (9) could then be generalized as,

$$\sin^2 \theta_i = A\alpha_i + D\delta_i, \quad (10)$$

where  $A = \frac{\lambda^2}{4a_0^2}$ ,  $\alpha_i = h_i^2 + k_i^2 + l_i^2$ , and  $\delta_i = \sin^2 2\theta_i$ .

By combining Cohen's method with the least square approach [41], the optimum values of the coefficients  $A$  and  $D$  in Eq. (10) could be obtained by minimizing  $f(A, D)$ ,

$$f(A, D) = \sum_i (\sin^2 \theta_i - A\alpha_i - D\delta_i)^2. \quad (11)$$

Hence, the minimization condition was applied,

$$\frac{\partial f(A, D)}{\partial A} = \frac{\partial f(A, D)}{\partial D} = 0, \quad (12)$$

leading to a system of two equations,

$$\begin{cases} A \sum_i \alpha_i^2 + D \sum_i \alpha_i \delta_i = \sum_i \sin^2 \theta_i \alpha_i \\ A \sum_i \alpha_i \delta_i + D \sum_i \delta_i^2 = \sum_i \sin^2 \theta_i \delta_i \end{cases} \quad (13)$$

Data needed to resolve the system of Eq. (13) was determined from the XRD patterns in Fig. 6 and was summarized in Table 1. This system was solved twice for the base alloy and composite and using the obtained values of  $A$  (i.e.,  $A = \frac{\lambda^2}{4a_0^2}$ ),  $a_0$  was then calculated to be 4.059 Å for the 2024Al and 4.051 Å for the 2.0 wt.% CNT/2024Al composite. While the lattice parameter for the 2.0 wt.% CNT/2024Al composite could not be found in the literature, the lattice

parameter  $a_0$  for 2024Al alloy was reported to be 4.06 Å [42], confirming the validity of the result obtained above. Jafari et al. [35] also measured the lattice parameter of 2024Al alloy aiming to understand better the effect of dissolution of Cu and Mg atoms in the Al lattice, and they obtained a value of 4.062 Å. The slight difference from the present result (i.e., 4.059 Å) could be related to the slightly different amounts (in wt.%) of alloying elements between the currently-studied Al2024 (4.5 Cu, 1.5 Mg, 0.6 Mn) and the Al2024 in Ref. [35] (4.1 Cu, 1.9 Mg, 0.5 Si).

The above finding about the decrease of the lattice parameter in the composite justifies the delay of the peaks shown in Fig. 6 due to the lattice shortening brought by the compressive micro-strains arising from the CNT addition. Qi and Wang [19] developed a model to link the lattice parameter to the volume fraction, size and shape of the nanoparticles in the metal matrix. A "shape factor" was introduced and was found to generate a 10% lattice change of the composite. The lattice parameter was also reported to decrease with increasing volume fraction of nanoparticles within the matrix [19]. Hence, an analogy could be made between the previous observations and the presently studied composite where the addition of 2.0 wt.% CNT resulted in a decrease of  $a_0$  as calculated above.

### 3.3. Crystallographic texture

Fig. 7 shows the {100}, {110} and {111} pole figures determined via XRD for the 2024Al alloy (Fig. 7(a),(f), and (k)) and the 2.0 wt.% CNT/2024Al composite (Fig. 7(c),(h), and (m)). A respective comparison was made with the pole figures obtained via EBSD for the 2024Al alloy (Fig. 7(b),(g), and (i)) and for the 2.0 wt.% CNT/2024Al composite (Fig. 7(d), (j), and (n)). It is seen that the two methods showed good agreement for both materials in terms of the location of major components and maximum intensities. Hence, based on either method the results obtained for the alloy and the composite revealed a similar texture. Standard texture components for FCC metals could be identified while examining the pole figures in Fig. 7. For instance, a closer look at the {100} pole figure revealed the presence of {112}<111> Copper texture [43] as illustrated in Fig. 7(e), based on the locations of the maximum intensities. The formation of the Copper type texture could be linked to the deformation process where internal reaction stresses were induced within the matrix as well as external shear stresses brought by the impact of the extrusion dies [44]. Based on Fig. 7(j), the {110} pole figure allowed identifying the {110}<001> Goss texture [45] known to occur as recrystallization texture in FCC materials [46]. This orientation was characterized by Wang et al. [47] as one of the main recrystallization texture components while studying the effect of rolling geometry on the mechanical properties of Al-Mg-Si alloys. Goss texture was also reported previously [48] while analyzing the crystallographic textures of 2024Al and 7034Al alloys via EBSD. The presence of Copper texture was further seen from the {111} pole figure where the location of the maximum intensities (Fig. 7(o)) characterized the {112}<111> Copper texture [43], corroborating the identification based on the {100} pole figure.

Texture strengthening for the 2.0 wt.% CNT/2024Al compared with the base alloy was detected to a certain extent in all pole figures. For example, the intensity of Copper texture increased from ~16.0 multiples of random distribution (MRD) for the 2024Al to ~17.1 MRD for the 2.0 wt.% CNT/2024Al as seen from the {111} pole figure. A less significant increase was observed for the Goss texture as seen from the {110} pole figure, from ~4.2 for the base alloy to ~4.4 MRD for the composite. The moderate texture strengthening by CNT additions shown in Fig. 7 confirmed the previous findings from the grain orientation map of the 2.0 wt.% CNT/2024Al composite (Fig. 1(b)) where a relatively strong <111> texture was observed (i.e., most of the grains along ED were oriented towards

**Table 1**

Cohen method parameters for the determination of lattice constants  $a_0$  of the 2024Al alloy and 2.0 wt.% CNT/2024Al composite, respectively.

Peak No	h	k	l	$2\theta/2024Al$	$2\theta/2.0 \text{ wt.\% CNT}/2024Al$
1	1	1	1	38.4830°	38.5285°
2	2	0	0	44.7367°	44.7742°
3	2	2	0	65.1062°	65.1579°
4	3	1	1	78.2396°	78.3086°
5	2	2	2	82.4390°	82.5975°

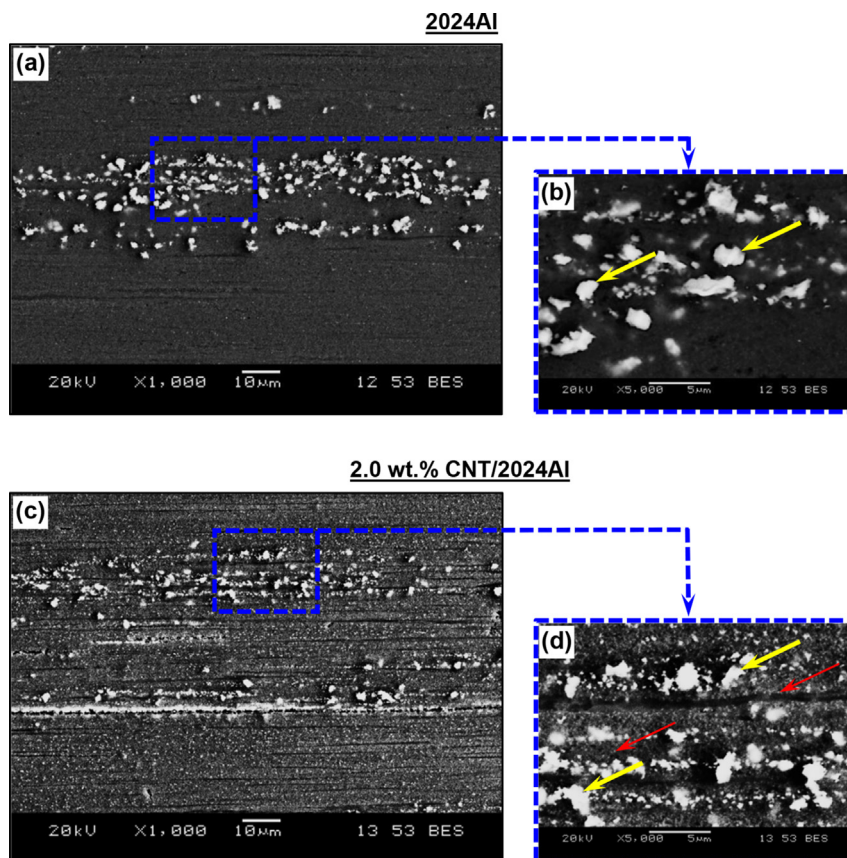


**Fig. 3.** Typical SEM micrographs showing the details of microstructural features of the 2024Al alloy and 2.0 wt.% CNT/2024Al composite at (a, c) lower and (b, d) higher magnifications, respectively. Yellow coarse arrows indicate Cu-containing particles, and red thin arrows designate nanoparticles. (A colour version of this figure can be viewed online.)

and  $\text{Al}_2\text{Cu}$  peaks could be clearly observed in both materials, confirming the results presented previously in Fig. 4.

Some weak  $\text{Al}_4\text{C}_3$  peaks could also be identified from the XRD pattern of the composite, being in agreement with the TEM observations shown in Fig. 5(a). Similar results were reported by Bustamante et al. in the 0.5 to 5.0 wt.% CNT/2024Al composites [16,17], Jafari et al. in a 3.0 vol.% MWCNT/2024Al composite [31], Liu et al. in a 3.0 wt.% CNT/2009Al composite [8], and Kwon and Leparoux in a 1 vol.% CNT/Al composite [32]. In addition to  $\text{Al}_2\text{Cu}$  and  $\text{Al}_4\text{C}_3$  phases, Deng et al. [33] observed the formation of  $\text{Al}_2\text{CuMg}$  phase while studying Al composites with different CNT contents. The absence of this phase in the current study and other studies [8,16,17,31,32,34] could be attributed to (1) the lower diffusivity of bigger Mg atoms (atomic radius: 0.160 nm) in comparison with the Cu atoms (atomic radius: 0.128 nm) [31,35], and (2) the difference in the crystal structures of magnesium (HCP) and aluminum (FCC) matrix while copper and aluminum have the same FCC crystal structure. It should be noted that no carbon peaks were detected in the 2.0 wt.% CNT/2024Al composite, which could be due to the light atomicity of the CNT content, being too small to be detected by XRD [33]. That is, the amount of CNTs of <2.0 wt.% after the formation of some  $\text{Al}_4\text{C}_3$  phase was below the detection limit of XRD.

The presence of aluminum carbide  $\text{Al}_4\text{C}_3$  suggests the occurrence of reactions between Al and CNTs in the fabrication process where carbon atoms would easily react with Al at high temperatures at some defect locations [8,36]. The formation of  $\text{Al}_4\text{C}_3$  could also be related to the shortening of CNTs as shown in Fig. 5(a), leading to an increasing number of carbon atoms at the CNT tips

which would enhance the probability of CNT-Al reactions during severe plastic deformation at high temperatures. Bustamante et al. [16] showed the XRD results of CNT/2024Al composites as a function of CNT content, and observed that the magnitude of the  $\text{Al}_4\text{C}_3$  peaks increased with increasing CNT content, while the intensities of the  $\text{Al}_2\text{Cu}$  peaks varied less significantly. This was in good agreement with the XRD results shown in Fig. 6 about the appearance of small  $\text{Al}_4\text{C}_3$  peaks in the composite and the persistence of  $\text{Al}_2\text{Cu}$  compared with the base alloy. Jafari et al. [31] conducted the differential thermal analysis (DTA) on a 3 vol.% MWCNT/2024Al composite and observed an endothermic peak at 632 °C (i.e., the 2024Al melting) and an exothermic peak at 645–658 °C (i.e., the reaction between Al and CNTs) where  $\text{Al}_4\text{C}_3$  phase formed.

A close examination on the two XRD patterns in Fig. 6 revealed that the peaks of the 2.0 wt.% CNT/2024Al composite broadened with a lower intensity as well. This was attributed to the deformation, grain refinement and straining introduced by the CNTs [18]. In fact, the effects of grain size and strain on the peak broadening could be distinguished on the basis of the Williamson-Hall approach [37],

$$B \cos \theta = \frac{0.9\lambda}{d_g} + 2\varepsilon \sin \theta, \quad (1)$$

where  $B$  is the diffraction peak width at half-maximum intensity,  $2\theta$  is the Bragg diffraction angle,  $\lambda$  is the wavelength of the radiation used,  $d_g$  is the average grain size, and  $\varepsilon$  is the average internal strain. It is clear from Eq. (1) that the increase of the bandwidth of the

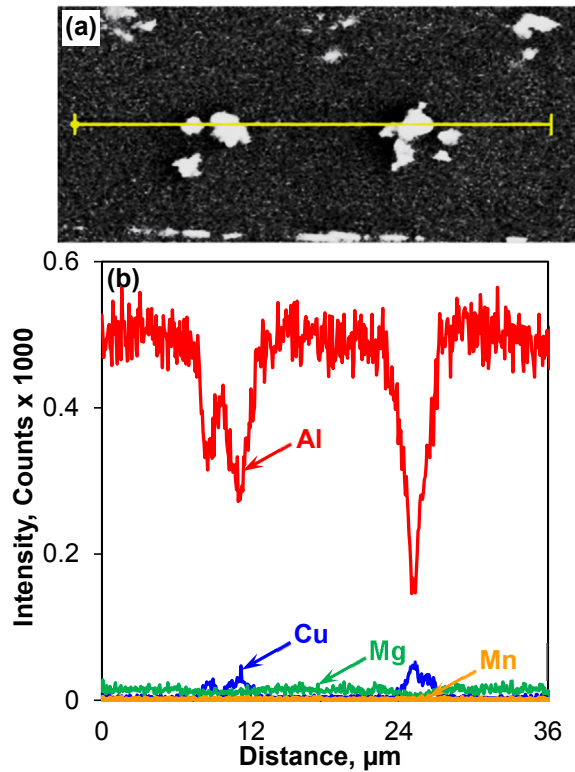


Fig. 4. (a) A typical SEM back-scattered electron image, and (b) EDS line scan results across a position indicated by the line in (a) for the 2.0 wt.% CNT/2024Al composite. (A colour version of this figure can be viewed online.)

peaks for the 2.0 wt.% CNT/2024Al composite (Fig. 6) was due to further straining and grain size reduction expected from the addition of CNTs.

Another interesting feature observed in Fig. 6 was that the peaks for the alloy and composite were not perfectly centered, i.e., the peaks for the 2.0 wt.% CNT/2024Al composite were slightly delayed or shifted towards higher angles. In this context, Bustamante et al. [17] noted the impact of micro-strain on the distortion of the Al lattice because of the presence of CNTs. The lattice parameter  $a_0$  was therefore calculated in both the alloy and composite in the current study via Cohen's method [38] based on the least square

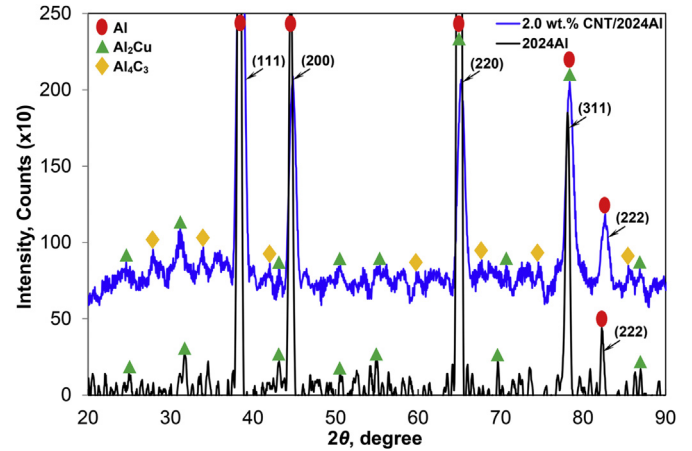


Fig. 6. X-ray diffraction patterns of the 2024Al alloy and 2.0 wt.% CNT/2024Al composite. (A colour version of this figure can be viewed online.)

refinement of the peak positions. According to the Bragg law,

$$\lambda = 2d \sin \theta, \quad (2)$$

where  $\lambda$  is the wavelength of the incident wave ( $\lambda = 1.540598 \text{ \AA}$  in the current study),  $d$  is the interplanar spacing and  $2\theta$  is the diffraction angle. By rearranging Eq. (2) one can write,

$$\ln(\sin^2 \theta) = \ln\left(\frac{\lambda^2}{4}\right) - 2 \ln d. \quad (3)$$

Differentiating Eq. (3) leads to,

$$\frac{\Delta \sin^2 \theta}{\sin^2 \theta} = -2 \frac{\Delta d}{d}, \quad (4)$$

where  $\Delta d/d$  is known as the systematic error, and is assumed to be in the form of,

$$\frac{\Delta d}{d} = K \cos^2 \theta, \quad (5)$$

where  $K$  is a constant [39].

Substituting Eq. (5) into Eq. (4),

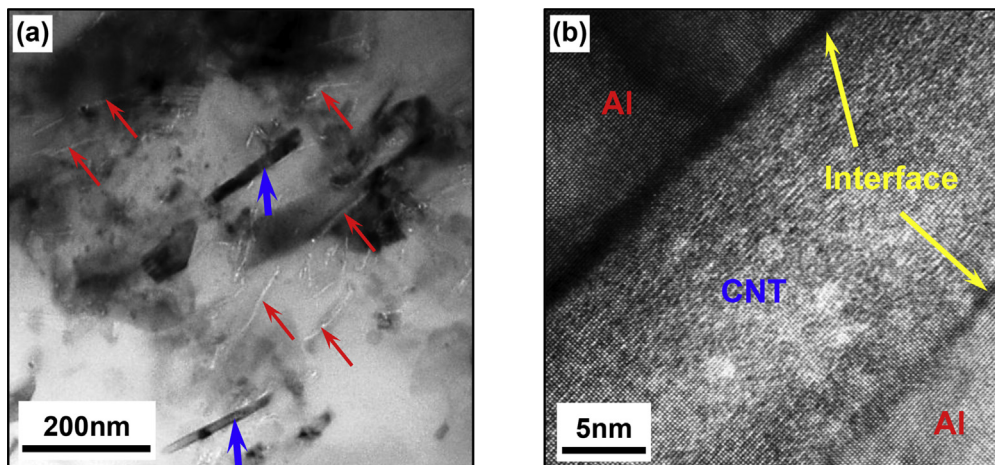
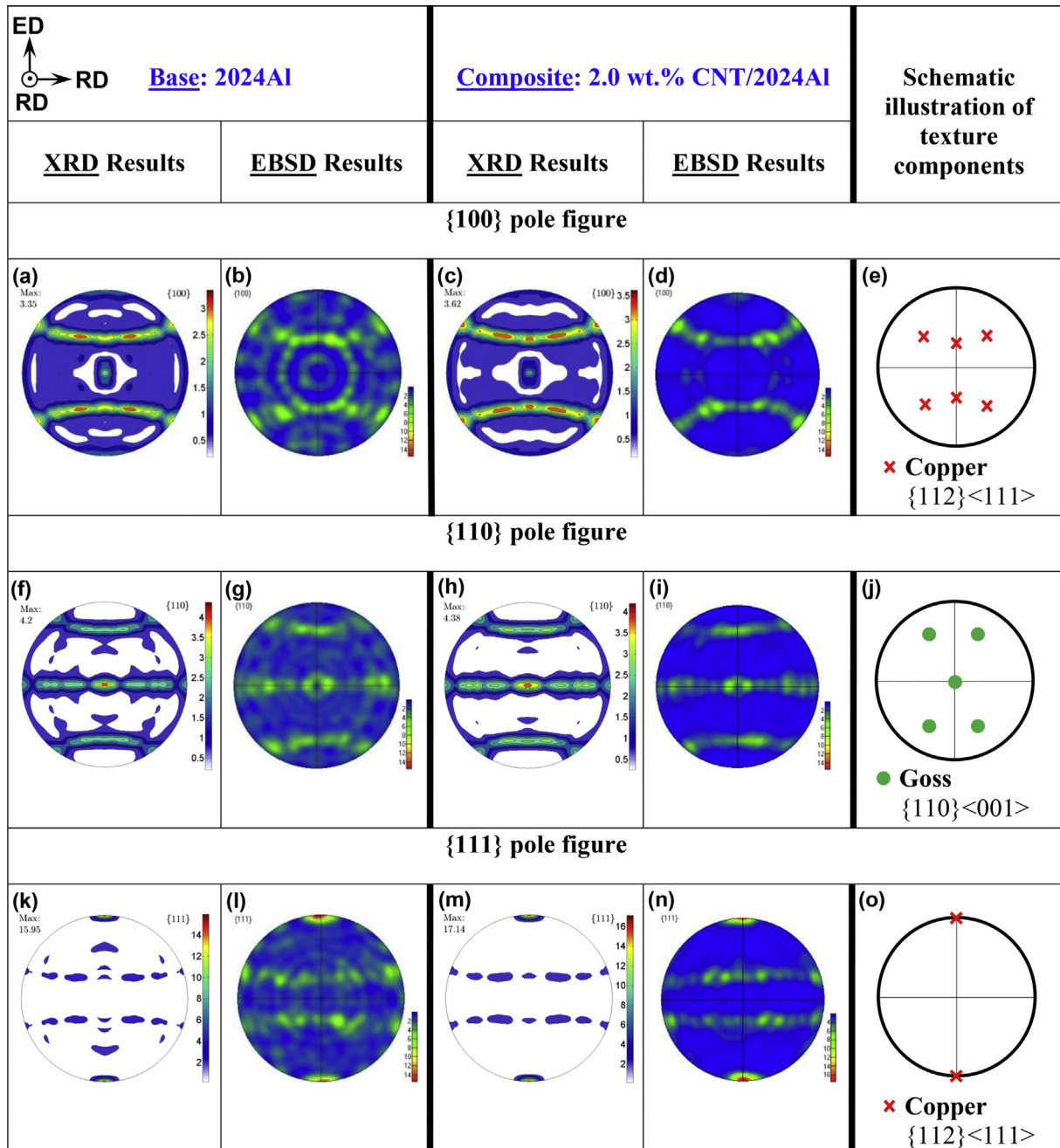


Fig. 5. (a) A typical TEM image of the 2.0 wt.% CNT/2024Al composite. Red thin arrows indicate singly dispersed CNTs, and blue thick arrows designate the  $\text{Al}_4\text{C}_3$  phase, (b) HRTEM image showing the interface structure between the Al matrix and CNTs. (A colour version of this figure can be viewed online.)



**Fig. 7.** {100}, {110}, and {111} pole figures of the 2024Al alloy based on (a, f, k) XRD results and (b, g, l) EBSD results along with the 2.0 wt.% CNT/2024Al composite based on (c, h, m) XRD results and (d, i, n) EBSD results, respectively, where ED stands for the extrusion direction, and RD denotes the radial direction, and (e, j, o) indicate schematically the texture components. . (A colour version of this figure can be viewed online.)

the <111> direction by referring to the map color legend). Also, a few elongated grains previously observed in Fig. 1(b) were orientated towards the <001> direction which could be linked to the presence of the weaker {110}<001> Goss texture based on the texture component identified in Fig. 7(j).

It should be noted that depending on the type of reinforcement and the initial texture, the strengthening of base alloy could lead to either stronger or weaker texture [20,46,49–52]. Both scenarios have been reported. For instance, Kocks et al. [46] studied the texture evolution while comparing a 8090Al base alloy with two different reinforced composites: (1) 15 vol.% SiC whiskers/8090Al, and (2) 15 vol.% SiC particles/8090Al. The intensity of texture

became weaker in the SiC whisker reinforced composite, and stronger in the SiC particle reinforced composite, with respect to the base alloy. This observation underlines the impact of the type of reinforcement on the texture development, suggesting that the particles are not as effective as whiskers at repressing the texture [46]. Habibi et al. [49] compared the texture evolution of monolithic Mg to a hybrid Mg/0.50Al-0.18CNT nanocomposite. Texture evolution was quantified by means of  $I/I_{max}$ , where  $I_{max}$  was defined as the maximum intensity on the observed plane.  $I/I_{max}$  increased from 0.96 for Mg, to 1.00 for Mg/0.50Al-0.18CNT along the (10 $\bar{1}$ 0) prismatic plane. A different trend was observed along the (10 $\bar{1}$ 1) pyramidal plane where  $I/I_{max}$  decreased from 1.00 for Mg, to 0.98

for Mg/0.50Al-0.18CNT. Hence, they reported the presence of both texture “hardening” and “softening” which they assumed strongly reliant on the CNT content. In another investigation, Habibi et al. [50] proved that the strengthening of a material could be achieved through the texture hardening.

The conditions favoring stronger textures in the composite were previously discussed by Engler et al. [51] and were attributed to the additional nanoparticles present in the composite (Fig. 3(c) and (d)) in comparison with the base alloy having only the coarser Cu-containing particles (Fig. 3(a) and (b)). Dislocation movement is strongly hindered by the nanoparticles since the “geometrically necessary dislocations” at the matrix/nanoparticle interface have to be stored to accommodate the strain incompatibilities. Hence, due to their nano-size and their partial coherency, nanoparticles facing a high dislocation density are “cut” by these dislocations, so that local softening and strongly localized slip on only a few preferred slip systems will take place [51]. This will lead to less effective “constraints” for the deformation imposed by the surrounding grains, thus only the most favorably oriented slip systems will be active, resulting in a stronger preferred orientation [52]. Such a slip localization would result in an “incompatible deformation” at the grain boundaries which can only be compensated locally, further responsible for the observed texture effects in the nanoparticle-containing composite [51]. Compared with the 2024Al base alloy, the presence of CNTs in the composite leads to the restriction of slip by the very small inter-particle spaces, which causes a locally “very homogeneous” deformation and an increased rate of texture development [52].

### 3.4. Compressive behavior

Fig. 8 shows the true stress-true strain compression curves of the base alloy and the composite obtained at different temperatures and strain rates. In Fig. 8(a) tests were held at RT while varying the strain rates (i.e., 0.1, 0.01, and  $0.001\text{ s}^{-1}$ ), whereas in Fig. 8(b) test temperatures were varied (i.e., RT, 200, 300, and  $400\text{ °C}$ ) at a fixed strain rate of  $0.001\text{ s}^{-1}$ . A comparison between both plots affirms that the test temperature had a stronger effect on the deformation curves of both materials, with respect to the effect of strain rate at RT. Overall, the flow stress increased considerably as the true strain increased during the initial stages of deformation at RT. Once the peak value was reached, a saturation level was attained regardless of the strain rate. A rise in the flow curves was observed for the 2024Al alloy with increasing strain rate.

Fig. 9 represents the compressive yield strength (CYS) and ultimate compressive strength (UCS) of the base alloy and the composite as a function of strain rate at RT. Based on Fig. 9(a) and (b), the dependence of the CYS and UCS on the strain rate at RT was less noticeable in the case of the 2.0 wt.% CNT/2024Al composite. However, when comparing the two materials at a given strain rate (Fig. 8(a)), the strengthening behavior of CNTs was clearly demonstrated. This could be attributed to the Hall-Petch strengthening, also known as the GB strengthening where the material is strengthened by changing its average grain size due to the interaction between dislocations and GBs [53]. More details on the strengthening mechanisms due to CNT additions will be discussed in the coming section.

The enhancement of flow curves in the composite compared with the base alloy was also observed at all test temperatures at a fixed strain rate (Fig. 8(b)), indicating the importance of CNT reinforcement in the improvement of the mechanical properties. Similarly, Choi et al. [54] also observed the improvement in the flow resistance by the addition of CNTs while studying composites with different volume fractions of MWCNTs (i.e., 1.5, 3, 4.5 and 6 vol.%) at different temperatures. The evaluated CYS and UCS are shown in

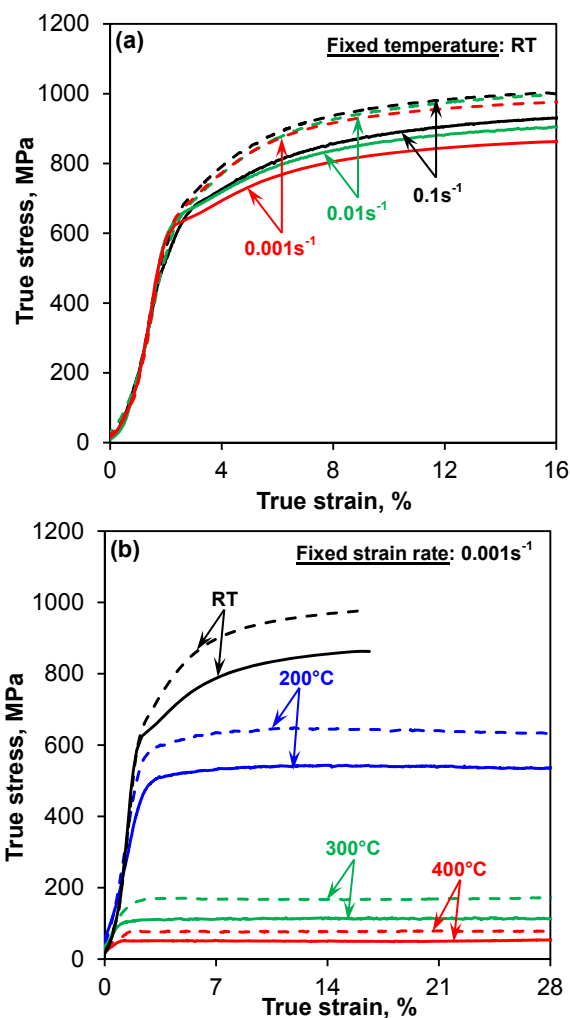


Fig. 8. Compressive true stress-true strain curves of the 2024Al alloy (continuous lines) and the 2.0 wt.% CNT/2024Al composite (dashed lines) (a) at room temperature (RT) and varying strain rates, and (b) at a fixed strain rate of  $0.001\text{ s}^{-1}$  and varying temperatures. (A colour version of this figure can be viewed online.)

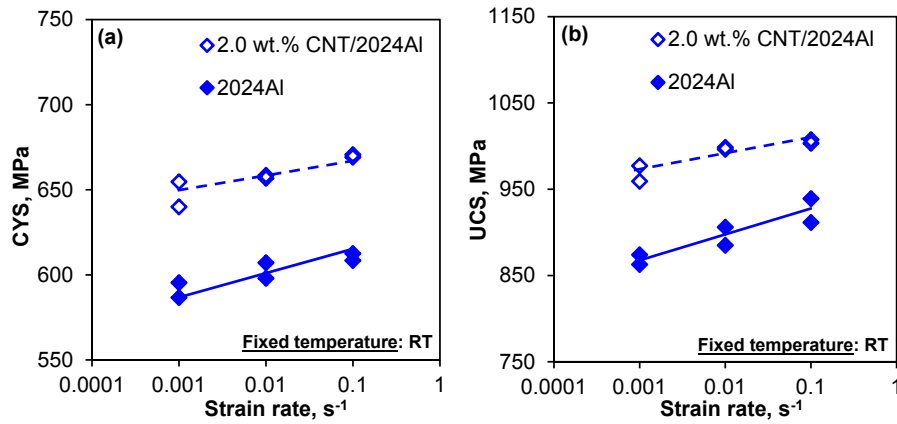
Fig. 10. Both CYS (Fig. 10(a)) and UCS (Fig. 10(b)) decreased with increasing temperature at a strain rate of  $0.001\text{ s}^{-1}$ . This could be attributed to the augmented thermal activation of the composite and the kinetic energy of the metal matrix which boosted the dislocation movements at higher temperatures [55], causing the observed decrease in Fig. 10(a) and (b).

Fig. 10(c) presents the hardening capacity of the 2.0 wt.% CNT/2024Al composite evaluated using the following equation [56].

$$H_c = \frac{\sigma_{UCS} - \sigma_{CYS}}{\sigma_{CYS}} \quad (14)$$

The hardening capacity ( $H_c$ ) of the composite was observed to first decrease from RT to  $300\text{ °C}$  and then increase slightly from  $300\text{ °C}$  to  $400\text{ °C}$  with increasing temperature. This could be explained by the gradual softening of the composite with increasing temperature. At  $400\text{ °C}$  the CYS became further lower relative to the decreasing UCS, giving rise to a higher hardening capacity based on Eq. (14), which indeed represented a more sensitive quantity of the CYS-UCS combination.

While no temperature dependence of the mechanical properties of CNT/2024Al composites was reported in the open literature, some limited studies on the effect of CNT amount on the



**Fig. 9.** Change of (a) compressive yield strength (CYS), and (b) ultimate compressive strength (UCS) with strain rate at room temperature for the 2024Al and the 2.0 wt.% CNT/2024Al composite. (A colour version of this figure can be viewed online.)

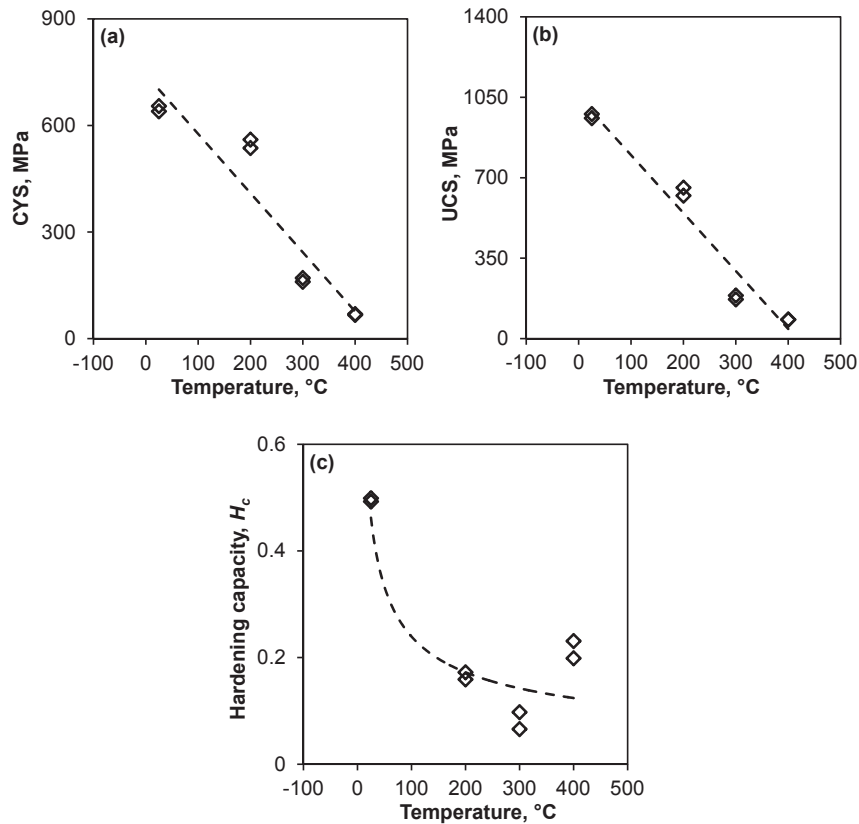


**Fig. 10.** Change of (a) compressive yield strength (CYS), (b) ultimate compressive strength (UCS), and (c) hardening capacity ( $H_c$ ) with temperature at a fixed strain rate of 0.001 s<sup>-1</sup> for the 2.0 wt.% CNT/2024Al composite.

mechanical properties at RT were seen. For instance, Bustamante et al. [16] studied the CNT/2024Al composites and reported a rapid increase in the mechanical properties as a function of the CNT addition. They showed that the composite with 3.0 wt.% CNTs, dispersed by mechanical milling and then sintering under argon atmosphere, was equivalent to the 2024Al-T6 tempered alloy, indicating that composites could eventually be enhanced further when a right temper was employed. On the other hand, Liu et al. [8] testified that for CNT/2009Al composites, increasing the CNT concentration from 1 to 3 wt.% led to a decrease in the strength and ductility. The opposing results obtained in the two studies could be

due to the difference in their processing conditions where CNT clusters and voids in the clusters might lead to the deterioration of mechanical properties [5,20,57]. The effectiveness of the fabrication processes for the current 2.0 wt.% CNT/2024Al alloy was clearly demonstrated in Fig. 8, where a significant improvement in the compressive properties of the composite at various temperatures and strain rates was achieved relative to the 2024Al base alloy, due to the homogenous dispersion of the CNTs in the Al matrix as shown in Fig. 5(a).

It is also noted that the CYS of the present base alloy at RT (Fig. 9(a)) was highly enhanced compared with the reported

strength of a conventional wrought Al2024 alloy (i.e., a tensile yield strength of ~324 MPa in T4 condition [58]). Various factors might have contributed to this improvement, mainly ball milling, which has resulted in a more refined microstructure than the conventional ingot metallurgy (IM) alloy reported in Ref. [58]. Ball milling leads to the generation of “high-strength” alloys, characterized by (1) better strength at RT, (2) improved elevated-temperature properties, and (3) increased stiffness and/or reduced density, allowing Al alloys to even compete with reinforced composites [58]. The improvement of the mechanical properties by ball milling has been documented by Choi et al. [59] who compared the YS of pure Al (unmilled) and pure Al (milled), while changing the milling time at a fixed strain rate of  $10^{-4} \text{ s}^{-1}$  at RT. The following values of YS were reported [59]: Al (unmilled), ~60 MPa; Al (milled-6 h), ~210 MPa; Al (milled-12 h), ~250 MPa; Al (milled-18 h), ~300 MPa; and Al (milled-24 h), ~380 MPa. The drastic improvement of YS between the milled and unmilled Al, even for the shortest milling time, could be explained by the major grain refinement credited to the Hall-Petch effect (i.e., GB strengthening) where by changing its average grain size, the material is strengthened due to the interaction between dislocations and GBs [35,53,60], leading to the observed higher YS values.

An additional reason that could eventually be considered and linked to the ball milling process is the spontaneous reaction between Al and O<sub>2</sub> when exposed to air during milling of the 2024Al powders, leading to the formation of Al<sub>2</sub>O<sub>3</sub> oxide. Spontaneous reactions between reduced aluminum powders (i.e., originally at a size of ~10 μm in the present work) and air have been previously acknowledged in Ref. [61]. Al<sub>2</sub>O<sub>3</sub> particles are then dispersed in the 2024Al matrix after extrusion, which could induce an increase in strength according to the Orowan strengthening mechanism [62] that will be explained later. Goujon et al. [61] also discussed the possibility of contamination due to the “wear” of the milling tools (i.e., the hardened steel balls of 5 mm in diameter in the present work). This could lead to the presence of Fe, Cr and Ni in the milled powders, mainly during the first 2 h of milling when the powder is still abrasive, hence leading to a further increase in the strength of the alloy [61]. Although T4 heat treatment was performed at the end, the hot extrusion process with a fairly high extrusion ratio (25:1), could cause a large plastic deformation and lead to an eventual increase in the dislocation density, further justifying the high CYS obtained in comparison with the YS of the conventional wrought 2024Al alloy reported in Ref. [58].

As mentioned above, the performed T4 heat treatment, consisting of a solution heat treatment (i.e., the dissolution of soluble phases), water cooling (i.e., the development of supersaturation), and natural age hardening (i.e., the precipitation of solute atoms at RT), can influence the UCS of base alloys and composites considerably [58]. Compared with a non-tempered alloy, the number of precipitates (i.e., Al<sub>2</sub>Cu particles in the current study) significantly increased in the T4 treated alloy, hence leading to further strengthening of the alloy. For instance, the tensile YS of a conventional wrought Al2024-T4 (~324 MPa [58]) was much higher than that of an annealed Al2024-O (~76 MPa [58]). As a result, the subsequent T4 treatment would further increase the compressive strength of the base alloy and composite (Fig. 9).

#### 4. Discussion: strengthening mechanisms

In this section various mechanisms that played a role in the enhancement of the reinforced composite and their significance will be discussed.

##### 4.1. Grain refinement and grain boundary strengthening

EBSD band contrast (BC) maps for the 2024Al alloy and the 2.0 wt.% CNT/2024Al composite, along with the respective distribution histograms of grain diameters, are shown in Fig. 11.

It is seen that the grain size was clearly smaller in the composite, where 2024Al had a diameter of ~5 μm for most grains (i.e., highest peak in Fig. 11(a)) with a grain size distribution up to ~11 μm. However, the 2.0 wt.% CNT/2024Al had a narrower range of variation where the highest peak of grain diameter was positioned at ~1 μm or less (Fig. 11(b)). The small portion of larger grain sizes in the histogram of the composite was due to the existence of elongated grains from the extrusion process (Fig. 1(b)). A clear grain refinement for the CNT reinforced 2024Al composite was hence attained. An analogy could be made with the results reported by Xiao et al. [63] where the grain size of a similar 2024Al matrix could be refined to 2–3 μm due to the addition of SiC reinforcing particles.

The impact of CNT addition on the grain refinement was well documented in the literature for MMCs. For instance, Suarez et al. [64] measured the mean grain size of a pure Ni, 1.0 wt.%, 2.0 wt.%, 3.0 wt.% and 5.0 wt.% MWCNT/Ni reinforced composites, and reported values of 47.6, 22.4, 4.9, 4.9, and 5.3 μm, respectively. Clearly, the grain size of the matrix was able to be refined once CNTs were added. The addition of CNTs up to 2.0 wt.% could decrease the grain size significantly, beyond which no further grain refinement was achieved. Thus, an “empirical reinforcement limit” at 2.0 wt.% MWCNT was specified [64]. Liu et al. [8] indicated that singly dispersed CNTs in the composite tended to be dispersed along GBs resulting in a much finer grain size. This could be linked to the results presented in Fig. 5(a), where TEM observations revealed singly dispersed CNTs. The impact of ball milling time on the grain refinement was further considered. Choi et al. [60] showed that their 3.0 vol.% MWCNT/2024Al could be refined even down to a grain size of 90 nm after a long time of 48 h of ball milling. The slightly larger grain size in the studied 2.0 wt.% CNT/2024Al in Fig. 11(b) (~1 μm or less) could be associated with a smaller amount of CNT addition (2.0 wt.% CNT) and a shorter ball milling time (6 h).

Based on the results shown in Fig. 11 and the results reported in the literature, it is necessary to understand the kinetics behind the grain refinement for the consolidated MMCs since it is one of the major reasons for the CYS increase previously observed in Figs. 8 and 9(a). Hall-Petch strengthening (i.e., GB strengthening) is directly linked to the CYS enhancement when the composite is strengthened by refining its average grain size [11,53,65]. The motion of dislocations during deformation is impeded by GBs due to the misorientation between neighboring grains. The smaller the grain size is, the more GBs are present, leading to a more difficult dislocation movement and thus a higher flow stress (Fig. 8). This is due to the fact that GBs act as “pinning points” prohibiting the dislocation movement and the eventual multiplication of dislocations. This leads to a “pile up” of dislocation clusters being unable to move past a boundary [66]. As pointed out by Keller et al. [67] the geometrically necessary dislocations could be rearranged into low-energy structures (i.e., substructures) characterized by their low angle grain boundaries (LAGBs). In this context, Fig. 12(a) displays the grain boundary mapping of the 2.0 wt.% CNT/2024Al along with the misorientation angle histogram (Fig. 12(b)). A bi-modal distribution is observed where a moderately important portion of the microstructure was characterized by LAGBs (i.e., angles of <10° in Fig. 12(a)) and an elevated peak of ~7° in Fig. 12(b)) which confirms the previously described kinetics of grain refinement. The presence of LAGBs would be associated with the formation of subgrains/substructures during ball milling. A majority of high angle grain boundaries (HAGBs) shown in Fig. 12 would be linked to the

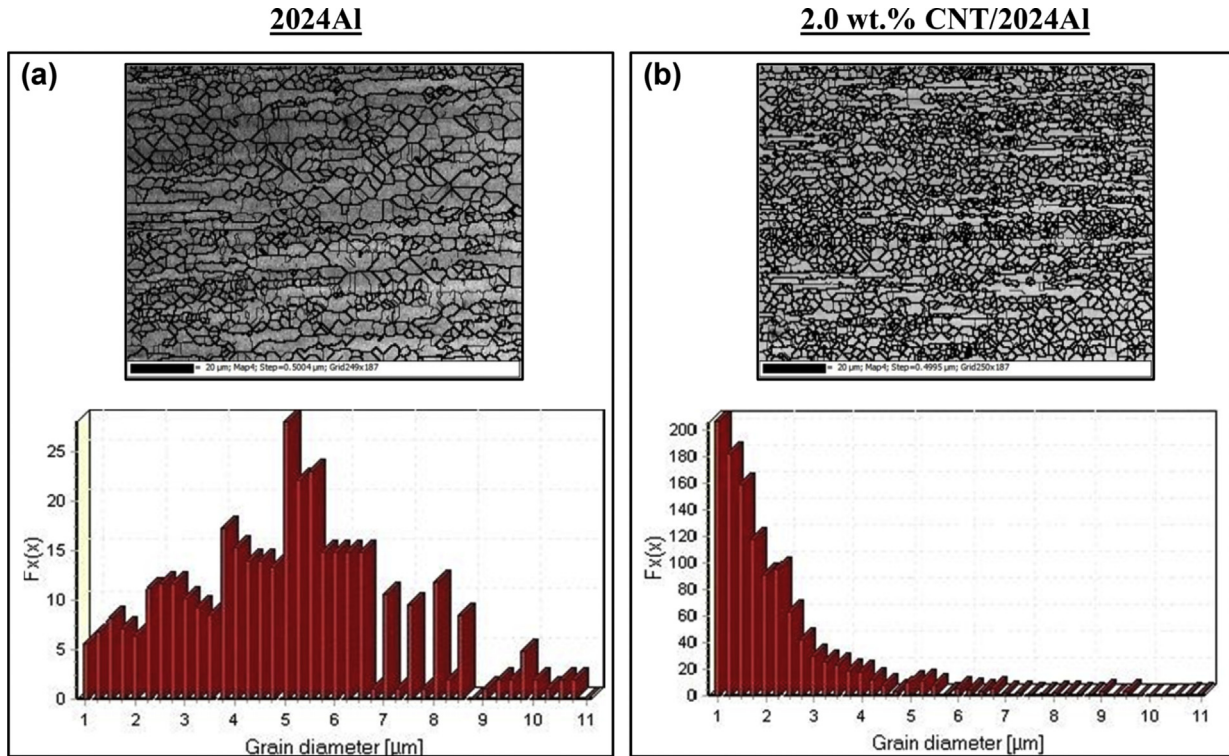


**Fig. 11.** EBSD band contrast maps along with the grain diameter distribution histograms for (a) the 2024Al alloy, and (b) the 2.0 wt.% CNT/2024Al composite. (A colour version of this figure can be viewed online.)

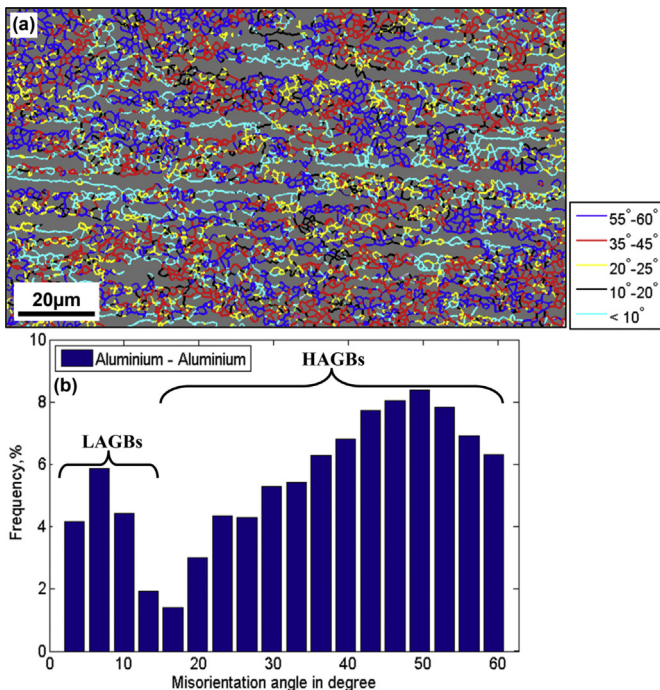


**Fig. 12.** (a) Grain boundary mapping along with (b) the misorientation angle histogram for the 2.0 wt.% CNT/2024Al composite. (A colour version of this figure can be viewed online.)

happening of recrystallization to be discussed in the coming section.

#### 4.2. Recrystallization and built-up substructures

Recrystallization is directly linked to the strengthening behavior of the composite since it is related to the evolution of grain microstructure in the CNT composites as described above and in the literature [68,69]. Various possible scenarios could lead to the occurrence of recrystallization, where the most common one is the formation and migration of HAGBs stemming from preexisting embryos [70]. This is in good agreement with the results observed in Fig. 12 about the dominance of misorientation angles  $>25^\circ$ . In other words, dislocation rearrangements leading to the formation of low dislocation density regions (associated with HAGBs) are capable of fast migration over the strained matrix [71].

Due to the existence of subgrains in the 2.0 wt.% CNT/2024Al composite as revealed by the LAGBs in Fig. 12, the nucleation of recrystallization by means of subgrain coalescence could also be another scenario. Earlier studies by Sandstrom et al. [72] introduced subgrain coalescence as the subgrain growth and the disappearance of sub-boundaries which lead to the decrease of the stored energy and the change of orientations between coalesced and neighboring subgrains. This promotes the formation of HAGBs having the ability to migrate fast and to form the recrystallization nucleus [73]. The happening of recrystallization by the migration of LAGBs (i.e., sub-boundaries) has been well documented in the literature dating back to the Cahn-Cottrell model [74,75].

#### 4.3. Zener drag effect

As shown in Figs. 1(a), 3 and 5(a), second-phase particles (i.e., nano-sized CNTs and Cu-containing particles) played an important role in controlling grain size and texture, in stimulating the nucleation of recrystallization and in pinning boundaries [76]. To move a boundary past a particle, a force has to be exerted which is

related to the size of the particle and the energy of the boundary [77]. In a random distribution of particles, the pinning force  $P_z$  exerted on the boundary could be given by Refs. [78],

$$P_z = \frac{3\gamma V_p}{2r}, \quad (15)$$

where  $\gamma$  is the grain boundary energy,  $V_p$  is the particle volume fraction and  $r$  is the particle radius. Based on Eq. (15), the presence of small and very closely spaced particles show retarded recrystallization, which happens to be reduced by the pinning effect of particles on both high and low angle GBs [73]. In the case of the studied 2.0 wt.% CNT/2024Al, the stagnation happened due to the motion restriction of GBs mainly by the CNTs which act as the pinning force or sometimes called “frictional forces” to the moving GBs, prohibiting the grain growth [64] and therefore leading to the grain refinement as observed in Fig. 11(b).

#### 4.4. Load transfer, thermal mismatch and Orowan looping

Load transfer, generation of dislocations by thermal mismatch, and Orowan looping were discussed in the literature as major mechanisms for the enhancement of the mechanical properties of CNT/Al reinforced composites [11,27,79,20]. These mechanisms were generally thought to occur simultaneously [80]. Similar to Zhang and Chen [27] and Mirza and Chen [11], Park et al. [80] also considered that the strength of the composite is the sum of each improvement (i.e., brought from each of the afore-mentioned mechanisms) plus the inherent strength of the matrix itself.

At the atomic level, a strong cohesion between the matrix and CNTs can be attained due to the nano-size of the reinforcement, leading to a direct bond between the matrix and reinforcement (Fig. 5(b)). Hence, depending on their volume fraction, nano-sized CNTs would carry a certain portion of the load (i.e., load transfer) between matrix and reinforcement [11,27]. The basis of the load transfer theory was initially introduced by Kelly and Tyson [28]. They stated that the applied stresses could be transferred to the reinforcements (e.g., CNTs) through interfacial shear stresses emanating from the matrix, which could be analyzed based on the shear lag model. In the case of the studied 2.0 wt.% CNT/2024Al, this could be justified by the formation of the  $Al_4C_3$  phase at the interface (Figs. 5 and 6). Similarly, Kwon et al. [29] and Bakshi and Agarwal [30] reported that the formation of  $Al_4C_3$  is necessary for an effective load transfer between the matrix and CNTs. Furthermore, SEM observations on the fracture surface shown in Fig. 13 revealed that the uniformly distributed CNTs were pulled out along with the presence of dimples, corroborating the happening of load transfer from the 2024Al matrix to CNTs.

The improved strength of the composite associated with the generation of dislocations by thermal mismatch is produced from

the “mismatch” in the coefficients of thermal expansions (CTEs) of the CNTs ( $\sim 1 \times 10^{-6} \text{ }^\circ\text{C}^{-1}$  [40]) and the 2024Al matrix ( $\sim 22.9 \times 10^{-6} \text{ }^\circ\text{C}^{-1}$  [40]), in the cooling phase of processing. This engenders the formation of dislocations in the Al matrix [11,27]. With increasing dislocation density in the matrix, the composite is strengthened which becomes one of the main mechanisms for the CYS improvement shown in Figs. 8 and 9(a). This improvement was attributed by George et al. [79] to the “prismatic punching” of dislocations at the interface, stimulating the work hardening of the matrix.

Due to their small diameter, CNTs were stated to be advantageous in terms of leading to a lower density of Griffith flaws [81] and a higher dislocation density generation, resulting in an increased strengthening. Furthermore, Orowan looping is generally considered when nano-sized CNTs obstruct the motion of dislocations, leading to the “dislocation bending” between the CNTs [82]. A back stress is therefore produced, preventing additional dislocation migration, and resulting in the augmentation of YS [11,27,79].

#### 4.5. Significance and relationships among the strengthening mechanisms

The significance of each of the mechanisms mentioned above in the total improvement of the CYS of the composite could be assessed based on the following equation [11],

$$\Delta\sigma_{C-Total} = \sqrt{(\Delta\sigma_{LT})^2 + (\Delta\sigma_{TM})^2 + (\Delta\sigma_{Orowan})^2 + (\Delta\sigma_{Hall-Petch-Zener})^2}, \quad (16)$$

where  $\Delta\sigma_{C-Total}$  is the total improvement in the CYS of the composite,  $\Delta\sigma_{LT}$  is the improvement in strength due to load transfer,  $\Delta\sigma_{TM}$  is associated with the improved strength due to the generation of dislocations by thermal mismatch,  $\Delta\sigma_{Orowan}$  is the strength improvement gained from the Orowan looping, and  $\Delta\sigma_{Hall-Petch-Zener}$  is the contribution brought by the Hall-Petch (fine grain) strengthening while accounting for the co-existing Zener drag effect. Each of the strengthening mechanisms introduced in the right-hand-side of Eq. (16) helps achieve the higher strength of the composite by enhancing the inherent strength of the matrix itself. Thus,

$$\sigma_{C-Total} = \sigma_M + \Delta\sigma_{C-Total}, \quad (17)$$

where  $\sigma_{C-Total}$  is the total strength of the composite, and  $\sigma_M$  is the strength of the matrix.

It should be noted that although there is no specific term for recrystallization in Eq. (16), its significance is implicitly accounted for since it is directly linked to the strengthening behavior of the

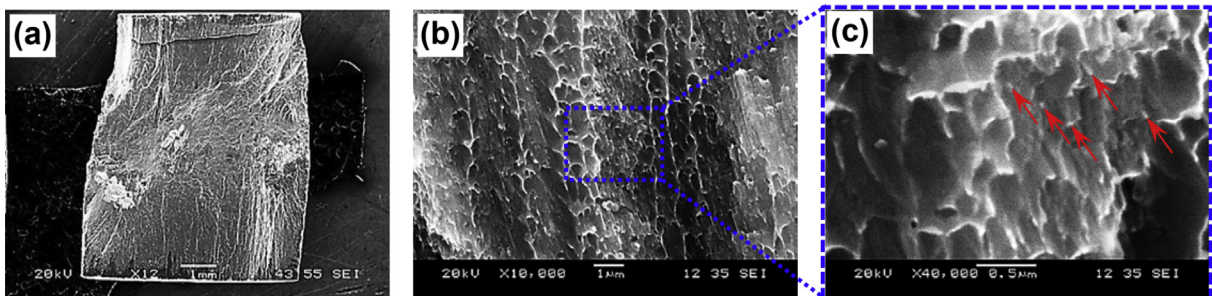


**Fig. 13.** SEM fractographs of (a) an overall fracture surface and (b, c) magnified views of the 2.0 wt.% CNT/2024Al sample compressed at RT at a strain rate of  $0.001 \text{ s}^{-1}$ . Red thin arrows indicate the pulled out CNTs. (A colour version of this figure can be viewed online.)

composite through the grain refinement [68]. As presented in Eq. (16), grain boundary (GB) strengthening is influential on the enhancement of CYS due to the refinement of the average grain size of the composite [53]. In addition to the load transfer, thermal mismatch and Orowan looping which are supposed to be present concurrently, the significance of the Hall-Petch effect was extended to account for the Zener pinning. As mentioned earlier, second-phase particles can impede the grain growth leading to a “pinned microstructure”. In this context, Mirza and Chen [11] additionally considered the “grain growth retardation” by the pinning of GBs due to the dispersed second phase particles in order to better accommodate the significance of various strengthening mechanisms in the enhancement of the CYS of the composite.

## 5. Conclusions

- 1) The addition of 2.0 wt.% CNTs in a 2024Al alloy led to fine grain sizes along with some Cu-containing second phase particles. TEM examinations revealed singly dispersed CNTs in the matrix, although the shortening of CNTs was observed to occur due to ball milling.
- 2) A bi-modal distribution of grain misorientation angles in the composite indicated the co-existence of mostly high-angle grain boundaries ( $\sim 50^\circ$ ) along with some low-angle grain boundaries ( $\sim 7^\circ$ ).
- 3) The presence of  $Al_4C_3$  phase, being either directly attached to CNTs or in the matrix in the neighborhood of CNTs, suggested the occurrence of reactions between the Al matrix and CNTs during the composite synthesis.
- 4) The X-ray diffraction peaks of the CNT reinforced composite were observed to be broadened due to the grain size reduction and compressive micro-strains brought by the CNT addition. The presence of compressive micro-strains also led to the lattice shortening.
- 5) The macro-texture determined via XRD and micro-texture via EBSD were observed to be in good agreement. Both revealed that the CNT reinforced composite contained stronger  $\{112\} <111>$  Copper texture and  $\{110\} <001>$  Goss texture than the 2024Al base alloy.
- 6) The deformation resistance (CYS and UCS) of the composite at both room and higher temperatures was effectively enhanced owing to the addition of CNTs. This was mainly associated with the mechanisms of Hall-Petch strengthening (i.e., significant grain refinement involving the Zener pinning effect of CNTs), and composite strengthening including load transfer, thermal mismatch and Orowan looping.

## Acknowledgments

The authors would like to thank the Natural Sciences and Engineering Research Council of Canada (NSERC) for providing financial support. This work was also financially supported by the National Basic Research Program of China (Nos. 2011CB932603 and 2012CB619600) and the CAS/SAFEA International Partnership Program for Creative Research Teams led by Professor Huiming Cheng (Institute of Metal Research, Chinese Academy of Sciences). One of the authors (D.L. Chen) is also grateful for the financial support by the Premier's Research Excellence Award (PREA), NSERC-Discovery Accelerator Supplement (DAS) Award, AUTO21 Network of Centers of Excellence, Canada Foundation for Innovation (CFI), and Ryerson Research Chair (RRC) program. The authors would also like to thank Messrs. A. Machin, Q. Li, C. Ma, J. Amankrah and R. Churaman for easy access to the laboratory facilities of Ryerson University and their assistance in the experiments.

## References

- [1] N. Behabtu, C.C. Young, D.E. Tsentlovich, O. Kleinerman, X. Wang, W. Anson, et al., Strong, light, multifunctional fibers of carbon nanotubes with ultrahigh conductivity, *Science* 339 (2013) 182–186.
- [2] P.M. Ajayan, J.M. Tour, Materials science: nanotube composites, *Nature* 447 (2007) 1066–1068.
- [3] J.D.W. Madden, Stiffer than steel, *Science* 323 (2009) 1571–1572.
- [4] M.M. Shulaker, G. Hills, N. Patil, H. Wei, H.Y. Chen, H.S.P. Wong, S. Mitra, Carbon nanotube computer, *Nature* 501 (2013) 526–530.
- [5] Y. Huang, Q. Ouyang, D. Zhang, J. Zhu, R. Li, H. Yu, Microstructures and tensile properties of ultrafine-grained Ni–(1–3.5) wt% SiCNP composites prepared by a powder metallurgy route, *Acta Metall. Sin.* 27 (2014) 775–786.
- [6] T. Kuzumaki, K. Miyazawa, H. Ichinose, K. Ito, Processing of carbon nanotube reinforced aluminum composite, *J. Mater. Res.* 13 (1998) 2445–2449.
- [7] R.P. Bustamante, F.P. Bustamante, I.E. Guel, C.R.S. Rodriguez, J.A.M. Aquino, J.M.H. Ramirez, et al., Characterization of Al2024-CNTs composites produced by mechanical alloying, *Powder Technol.* 212 (2011) 390–396.
- [8] Z.Y. Liu, B.L. Xiao, W.G. Wang, Z.Y. Ma, Singly dispersed carbon nanotube/aluminum composites fabricated by powder metallurgy combined with friction stir processing, *Carbon* 50 (2012) 843–852.
- [9] S. Dong, J. Zhou, D. Hui, A quantitative understanding on the mechanical behaviors of carbon nanotube reinforced nano/ultrafine-grained composites, *Int. J. Mech. Sci.* 101 (2015) 29–37.
- [10] P. Barai, G.J. Weng, The competition of grain size and porosity in the viscoplastic response of nanocrystalline solids, *Int. J. Plast.* 24 (2008) 1380–1410.
- [11] F.A. Mirza, D.L. Chen, A unified model for the prediction of yield strength in particulate-reinforced metal matrix nanocomposites, *Materials* 8 (2015) 5138–5153.
- [12] N. Silvestre, B. Faria, J.N.C. Lopes, Compressive behavior of CNT-reinforced aluminum composites using molecular dynamics, *Compos. Sci. Tech.* 90 (2014) 16–24.
- [13] H.J. Choi, G.B. Kwon, G.Y. Lee, D.H. Bae, Reinforcement with carbon nanotubes in aluminum matrix composites, *Scr. Mater.* 59 (2008) 360–363.
- [14] S.R. Bakshi, A.K. Keshri, A. Agarwal, A comparison of mechanical and wear properties of plasma sprayed carbon nanotube reinforced aluminum composites at nano and macro scale, *Mater. Sci. Eng. A* 528 (2011) 3375–3384.
- [15] N. Saheb, Compressive behavior of spark plasma sintered CNT reinforced Al2124 and Al6061 nanocomposites, *Adv. Mater. Res.* 652 (2013) 33–37.
- [16] R.P. Bustamante, F.P. Bustamante, W.A. Flores, J.M.H. Ramirez, Al2024-CNTs composites by mechanical alloying, *Microsc. Microanal.* 16 (2010) 1256–1257.
- [17] R.P. Bustamante, F.P. Bustamante, I.E. Guel, L.L. Jimenez, M.M. Yoshida, R.M. Sanchez, Effect of milling time and CNT concentration on hardness of CNT/Al2024 composites produced by mechanical alloying, *Mater. Charact.* 75 (2013) 13–19.
- [18] X.N. Hao, H.P. Zhang, R.X. Zheng, Y.T. Zhang, K. Ameyama, C.L. Ma, Effect of mechanical alloying time and rotation speed on evolution of CNTs/Al-2024 composite powders, *J. Nonferr. Metal. Soc. China* 24 (2014) 2380–2386.
- [19] W.H. Qi, M.P. Wang, Size and shape dependent lattice parameters of metallic nanoparticles, *J. Nanopart. Res.* 7 (2005) 51–57.
- [20] G. Fan, R. Xu, Z. Tan, D. Zhang, Z. Li, Development of flake powder metallurgy in fabricating metal matrix composites: a review, *Acta Metall. Sin.* 27 (2014) 806–815.
- [21] H. Wei, Z. Li, D.B. Xiong, Z. Tan, G. Fan, Z. Qin, et al., Towards strong and stiff carbon nanotube-reinforced high-strength aluminum alloy composites through a microlaminated architecture design, *Scr. Mater.* 75 (2014) 30–33.
- [22] J. Liao, M.J. Tan, R.V. Ramanujan, S. Shukla, Carbon nanotube evolution in aluminum matrix during composite fabrication process, *Mater. Sci. Forum* 690 (2011) 294–297.
- [23] J. Guo, S. Amira, P. Gougeon, X.G. Chen, Effect of the surface preparation techniques on the EBSD analysis of a friction stir welded AA1100-B 4 C metal matrix composite, *Mater. Charact.* 62 (2011) 865–877.
- [24] Y. Zhao, H.L. Suo, M. Liu, D. He, Y.X. Zhang, L. Ma, et al., Highly reinforced and cube textured Ni alloy composite substrates by a hybrid route, *Acta Mater.* 55 (2007) 2609–2614.
- [25] R. Bauri, D. Yadav, C.N. Shyam Kumar, B. Balaji, Tungsten particle reinforced Al5083 composite with high strength and ductility, *Mater. Sci. Eng. A* 620 (2015) 67–75.
- [26] F. Mokdad, D.L. Chen, Cyclic deformation and anelastic behavior of ZEK100 magnesium alloy: effect of strain ratio, *Mater. Sci. Eng. A* 640 (2015) 243–258.
- [27] Z. Zhang, D.L. Chen, Consideration of Orowan strengthening effect in particulate-reinforced metal matrix nanocomposites: a model for predicting their yield strength, *Scr. Mater.* 54 (2006) 1321–1326.
- [28] A. Kelly, W.R. Tyson, Tensile properties of fibre reinforced metals, *J. Mech. Phys. Solids* 13 (1965) 329–350.
- [29] H. Kwon, M. Estili, K. Takagi, T. Miyazaki, A. Kawasaki, Combination of hot extrusion and spark plasma sintering for producing carbon nanotube reinforced aluminum matrix composites, *Carbon* 47 (2009) 570–577.
- [30] S.R. Bakshi, A. Agarwal, An analysis of the factors affecting strengthening in carbon nanotube reinforced aluminum composites, *Carbon* 49 (2011) 533–544.
- [31] M. Jafari, M.H. Abbasi, M.H. Enayati, F. Karimzadeh, Mechanical properties of nanostructured Al2024–MWCNT composite prepared by optimized

- mechanical milling and hot pressing methods, *Adv. Powder Technol.* 23 (2012) 205–210.
- [32] H. Kwon, M. Leparoux, Hot extruded carbon nanotube reinforced aluminum matrix composite materials, *Nanotechnology* 23 (2012) 5701–5711.
- [33] C.F. Deng, D.Z. Wang, X.X. Zhang, A.B. Li, Processing and properties of carbon nanotubes reinforced aluminum composites, *Mater. Sci. Eng. A* 444 (2007) 138–145.
- [34] A.M.K. Esawi, K. Morsi, A. Sayed, M. Taher, S. Lanka, The influence of carbon nanotube (CNT) morphology and diameter on the processing and properties of CNT-reinforced aluminum composites, *Compos. Part A* 42 (2011) 234–243.
- [35] M. Jafari, M.H. Enayati, M.H. Abassi, F. Karimzadeh, Thermal stability and structural changes during heat treatment of nanostructured Al2024 alloy, *J. Alloy Compd.* 478 (2009) 260–264.
- [36] R. Andrews, D. Jacques, D. Qian, E.C. Dickey, Purification and structural annealing of multiwalled carbon nanotubes at graphitization temperatures, *Carbon* 39 (2001) 1681–1687.
- [37] G.K. Williamson, W.H. Hall, X-ray line broadening from filed aluminum and wolfram, *Acta Metall.* 1 (1953) 22–31.
- [38] B.D. Cullity, S.R. Stock, *Elements of X-Ray Diffraction*, third ed., Prentice Hall, New Jersey, 2001.
- [39] N.A. Razik, Precise lattice constants determination of cubic crystals from X-ray powder diffractometric measurements, *App Phys. A* 37 (1985) 187–189.
- [40] W.D. Callister Jr., D.G. Rethwisch, *Materials Science and Engineering: an Introduction*, ninth ed., John Wiley & Sons Inc, New York, 2014.
- [41] D.W. Marquardt, An algorithm for least-squares estimation of nonlinear parameters, *J. Soc. Ind. Appl. Math.* 11 (1963) 431–441.
- [42] C. Vijay, B. Song, D. Casem, *Dynamic Behavior of Materials*, Springer Science & Business Media, New York, 2012.
- [43] T.H. Courtney, *Mechanical Behavior of Materials*, Mc Graw-Hill, New York, 1990.
- [44] V. Randle, O. Engler, *Introduction to Texture Analysis: Macrotexture, Microtexture and Orientation Mapping*, CRC Press, New Yor, 2000.
- [45] H.R. Wenk, P. Van Houtte, Texture and anisotropy, *Rep. Prog. Phys.* 67 (2004) 1367–1428.
- [46] U.F. Kocks, C.N. Tome, H.R. Wenk, *Texture and Anisotropy: Preferred Orientations and Their Effect of Material Properties*, Cambridge University Press, United Kingdom, 2000.
- [47] X.F. Wang, M.X. Guo, L.Y. Cao, F. Wang, J.S. Zhong, L.Z. Zhuang, Effect of rolling geometry on the mechanical properties, microstructure and recrystallization texture of Al–Mg–Si alloys, *Int. J. Min. Metall. Mater.* 22 (2015) 738–747.
- [48] S.C. Wang, M.J. Starink, N. Gao, C. Xu, T.G. Langdon, Grain structure and texture development during ECAP of two heat-treatable Al-based alloys, *Rev. Adv. Mater. Sci.* 10 (2005) 249–255.
- [49] M.K. Habibi, M. Paramsothy, A.M.S. Hamouda, M. Gupta, Using integrated hybrid (Al + CNT) reinforcement to simultaneously enhance strength and ductility of magnesium, *Compos. Sci. Technol.* 71 (2011) 734–741.
- [50] M.K. Habibi, A.M.S. Hamouda, M. Gupta, Enhancing tensile and compressive strength of magnesium using ball milled Al+CNT reinforcement, *Compos. Sci. Technol.* 72 (2012) 290–298.
- [51] O. Engler, J. Hirsch, K. Lucke, Texture development in Al-1.8wt.% Cu depending on the precipitation state – I. Rolling textures, *Acta Metall. Mater.* 37 (1989) 2743–2753.
- [52] O. Engler, J. Hirsch, K. Lucke, Texture development in Al-1.8 wt.% Cu depending on the precipitation state – II. Recrystallization textures, *Acta Metall. Mater.* 43 (1994) 121–138.
- [53] W.S. Miller, F.J. Humphreys, Strengthening mechanisms in particulate metal matrix composites, *Scr. Mater.* 25 (1991) 33–38.
- [54] H.J. Choi, J.H. Shin, B.H. Min, J. Park, D.H. Bae, Reinforcing effects of carbon nanotubes in structural aluminum matrix nanocomposites, *J. Mater. Res.* 24 (2009) 2610–2616.
- [55] A.A. Khamei, K. Dehghani, R. Mahmudi, Modeling the hot ductility of AA6061 aluminum alloy after severe plastic deformation, *JOM* 67 (2015) 966–972.
- [56] N. Afrin, D.L. Chen, X. Cao, M. Jahazi, Strain hardening behavior of a friction stir welded magnesium alloy, *Scr. Mater.* 57 (2007) 1004–1007.
- [57] S. Simoes, F. Viana, M.A.L. Reis, M.F. Vieira, One-step synthesis and characterization of a nanocomposite based on carbon nanotubes/aluminum and its reinforcement effect on the metal matrix, *Compos. Struct.* 126 (2015) 114–122.
- [58] J.R. Davis, *Aluminum and Aluminum Alloys*, ASM International, 1993.
- [59] H.J. Choi, J.H. Shin, D.H. Bae, Grain size effect on the strengthening behavior of aluminum-based composites containing multi-walled carbon nanotubes, *Compos. Sci. Tech.* 71 (2011) 1699–1705.
- [60] H.J. Choi, B.H. Min, J.H. Shin, D.H. Bae, Strengthening in nanostructured 2024 aluminum alloy and its composites containing carbon nanotubes, *Compos. Part A* 42 (2011) 1438–1444.
- [61] C. Goujon, P. Goeuriot, P. Delcroix, G. Le Caer, Mechanical alloying during cryomilling of a 5000 Al alloy/AlN powder: the effect of contamination, *J. Alloys Compd.* 315 (2001) 276–283.
- [62] Y.C. Kang, S.L. Chan, Tensile properties of nanometric Al<sub>2</sub>O<sub>3</sub> particulate-reinforced aluminum matrix composites, *Mater. Chem. Phys.* 85 (2004) 438–443.
- [63] B. Xiao, Z.Y. Ma, J. Bi, Investigation on Superplasticity in SiCp/2024 Cold Rolling Sheet after Heat Treatment, *J. Mater. Sci. Technol.* 19 (2003) 382–384.
- [64] S. Suarez, E.R. Moore, B. Lechthaler, F. Mucklich, Grain growth analysis of multiwalled carbon nanotube-reinforced bulk Ni composites, *Carbon* 70 (2014) 173–178.
- [65] K.T. Kim, J. Eckert, S.B. Menzel, T. Gemming, S.H. Hong, Grain refinement assisted strengthening of carbon nanotube reinforced copper matrix nanocomposites, *Appl. Phys. Lett.* 92 (2008) 121901.
- [66] I. Daigo, Y. Terada, T. Sato, Effect of calcium additions on creep properties of a die-cast AM50 magnesium alloy, *Mater. Trans.* 49 (2008) 1957–1962.
- [67] R. Keller, W. Zielinski, W.W. Gerberich, On the onset of low-energy dislocation substructures in fatigue: grain size effects, *Mater. Sci. Eng. A* 113 (1989) 267–280.
- [68] A.H. Feng, Z.Y. Ma, Enhanced mechanical properties of Mg–Al–Zn cast alloy via friction stir processing, *Scr. Mater.* 56 (2007) 397–400.
- [69] R.S. Mishra, Z.Y. Ma, Friction stir welding and processing, *Mater. Sci. Eng. R* 50 (2005) 1–78.
- [70] H.R. Ezatpour, A. Chaichi, S.A. Sajjadi, The effect of Al<sub>2</sub>O<sub>3</sub>-nanoparticles as the reinforcement additive on the hot deformation behavior of 7075 aluminum alloy, *Mater. Des.* 88 (2015) 1049–1056.
- [71] P.A. Beck, P.R. Sperry, Strain induced grain boundary migration in high purity aluminum, *J. Appl. Phys.* 21 (1950) 150–152.
- [72] R. Sandstrom, B. Lehtinen, E. Hedman, I. Groza, S. Karlsson, Subgrain growth in Al and Al-1% Mn during annealing, *J. Mater. Sci.* 13 (1978) 1229–1242.
- [73] P.R. Rios, F. Siciliano Jr., H.R.Z. Sandim, R.L. Plaut, A.F. Padilha, Nucleation and growth during recrystallization, *Mater. Res.* 8 (2005) 225–238.
- [74] R.W. Cahn, A new theory of recrystallization nuclei, *Proc. Phys. Soc.* 63 (1950) 232–236.
- [75] A.H. Cottrell, Theory of dislocations. *Progress in metal physics*, *Proc. Metal. Phys.* 4 (1953) 251–255.
- [76] F.J. Humphreys, M. Heatherly, *Recrystallization and Related Annealing Phenomena*, Pergamon Press, Oxford, 1995.
- [77] W.J. Kim, Y.J. Yu, The effect of the addition of multiwalled carbon nanotubes on the uniform distribution of TiC nanoparticles in aluminum nanocomposites, *Scr. Mater.* 72 (2014) 25–28.
- [78] E. Nes, N. Ryum, O. Hunderi, On the Zener drag, *Acta Metall.* 33 (1985) 11–22.
- [79] R. George, K.T. Kashyap, R. Rahul, S. Yamdagni, Strengthening in carbon nanotube/aluminum (CNT/Al) composites, *Scr. Mater.* 53 (2005) 1159–1163.
- [80] J.G. Park, D.H. Keum, Y.H. Lee, Strengthening mechanisms in carbon nanotube-reinforced aluminum composites, *Carbon* 95 (2015) 690–698.
- [81] H. Yin, H.J. Qi, F. Fan, T. Zhu, B. Wang, Y. Wei, Griffith criterion for brittle fracture in graphene, *Nano Lett.* 15 (2015) 1918–1924.
- [82] Q. Li, C.A. Rottmair, R.F. Singer, CNT reinforced light metal composites produced by melt stirring and by high pressure die casting, *Compos. Sci. Tech.* 70 (2010) 2242–2247.